J Nanostruct 16(4): 4913-4926, Autumn 2026

RESEARCH PAPER

Sawdust-Derived Biochar and Ag_2O Nanoparticles for Adsorptive Desulfurization of Iraqi Crude Oil: Temperature-Resolved Kinetics, Diffusion Control and Thermodynamics

Wedad Nasser Aday *, *Abdulqadier Hussien Al-Khazraji*

Department of Chemistry, College of Education for Pure Science, University of Diyala, Diyala, Iraq

ARTICLE INFO

Article History:
Received 19 May 2026
Accepted 28 July 2026
Published 01 October 2026

Keywords:
Adsorptive desulfurization
Ag_2O nanoparticles
Elovich kinetics
Intraparticle diffusion
Iraqi crude oil
Sawdust biochar

ABSTRACT

Removing sulfur from crude oil by adsorption is still an attractive option, mainly because the process runs at atmospheric pressure and consumes no hydrogen. In the present work a biochar (BC) obtained from local sawdust, Ag_2O nanoparticles (Ag_2O NPs) and an Ag_2O/BC binary composite were prepared and evaluated against a model oil prepared from Basra crude diluted with n-hexane, with an initial sulfur content of 2.9 wt%. X-ray diffraction confirmed the crystallinity of the Ag_2O phase with a face-centred cubic lattice (a = 4.086 Å) and a mean Scherrer crystallite size of 30.5 nm. The char retained a broad amorphous carbon feature near 23° together with calcite and quartz reflections inherited from the feedstock ash. Nitrogen physisorption gave specific surface areas of 340, 407 and 441 $m^2\ g^{-1}$ for Ag_2O NPs, BC and Ag_2O/BC respectively, with mean pore widths close to 2.3 nm in all three cases. Batch kinetics were measured at 293 K between 30 and 150 min, and the effect of temperature was studied separately at 298–353 K. Uptake was endothermic for every solid: at 293 K and 150 min, removal reached 85.9% for BC, 68.3% for the Ag_2O NPs and 52.1% for the composite, while raising the temperature to 353 K at 60 min contact time increased BC removal to 88.6%. Contrary to what the surface-area data alone would suggest, depositing Ag_2O on the char reduced performance under all conditions tested, which we attribute mainly to partial pore blocking. At 293 K the Elovich equation described the kinetics well (R^2 = 0.94–0.98) whereas the pseudo-second-order model did not, and Weber–Morris plots resolved two linear regions with non-zero intercepts. Adsorption was endothermic (ΔH = 21.7–49.3 kJ mol^{-1}) and the biochar was the only material for which $\Delta G°$ became negative, above 313 K.

How to cite this article
Aday W., Al-Khazraji A. Sawdust-Derived Biochar and Ag_2O Nanoparticles for Adsorptive Desulfurization of Iraqi Crude Oil: Temperature-Resolved Kinetics, Diffusion Control and Thermodynamics. J Nanostruct, 2026; 16(4):4913-4926. DOI: 10.22052/JNS.2026.04.037

INTRODUCTION

One of the more difficult problems facing refiners are the sulphur compounds in crude oil. They are once burnt and they exit the stack as SOx and poison catalysts and target steel within the plant [1,2]. Hydrodesulfurization of mercaptans and sulphides is easy but the sterically hindered thiophenic species, particularly dibenzothiophene and its alkylated derivatives can only be converted under harsh conditions and enormous amounts of hydrogen [2,3]. This is why adsorption has kept the

* *Corresponding Author Email: wedadnaser25@gmail.com*

attention of a good number of groups: it runs at or near ambient conditions, it does not touch the octane number, and the equipment is simple [3,4].

Cost, however, remains the sticking point. Commercial activated carbons and zeolites are effective but expensive, so a substantial literature has grown around chars made from agricultural and forestry residues. Date and olive stones [1], date pits [5], walnut shells [6], rice husk [7], banana peel [8], corn cobs [9], corncob [10] and cashew nut shell [11] have all been converted into adsorbents with reasonable sulfur capacity. Sawdust is abundant in Iraq and, as far as we are aware, has not been examined for crude oil desulfurization, although it has been used for other pollutants.

A second line of work aims at raising selectivity by anchoring metals or metal oxides on the carbon. Zn and Mn on corn cob carbon [9], Cu and Mn on activated charcoal [12,13], Fe3O4 and MnO2 on palm kernel shell carbon [14], CuO on date pit char [5] and Ni on carbon beads [15] have all been reported to improve removal relative to the bare support. Ag_2O is of particular interest here because Ag(I) forms pi-complexes with thiophenic rings; Ag/ZnO on activated carbon reached 99% DBT removal [16], silver-coated membranes gave 70-79% from a diesel model [17], and Ag nanoparticles in porous aromatic frameworks were recently shown to release adsorbed sulfur under illumination through their plasmon resonance [18].

What is less often reported is the case where loading a metal fails to help. Most of the published works show the changed material as a superior adsorbent, but negative results of this type are rarely presented. However, they convey information about the real behaviour of these composites. The experiment described below started as a simple comparison of sawdust biochar, Ag2O nanoparticles and their composite and developed into an attempt to understand why the composite performed poorest. The kinetics were studied at four temperatures rather than one, allowing the separation of the diffusion phases and the activation barrier.

MATERIALS AND METHODS

Materials

Silver nitrate (99.0%), sodium hydroxide (98.0%), absolute ethanol (99.9%) and n-hexane were of analytical grade and used as received. Deionized water was used throughout. Sawdust was collected from carpentry workshops in Diyala Governorate, washed several times with tap and then deionized water to remove dust and resin, and dried in open air. Crude oil was taken from the Basra oil fields in southern Iraq and kept in sealed amber bottles at 4 C until use; its total sulfur content was 2.9 wt%.

Preparation of sawdust biochar

The washed and sun-dried sawdust was loaded into a covered ceramic crucible and placed in a muffle furnace. Pyrolysis was carried out at 700 C for 3 h under a nitrogen blanket, the crucible lid and a continuous N2 purge being used to keep the atmosphere oxygen-poor. After the furnace had cooled to room temperature the char was ground in an agate mortar, passed through a 100-mesh sieve and stored in a desiccator. The yield was around 1/3 of the initial mass, as expected for slow pyrolysis of woody biomass at this temperature.

Preparation of Ag_2O nanoparticles

Ag_2O nanoparticles were obtained by alkaline precipitation. In a 500 mL beaker, 1 g of $AgNO_3$ was dissolved in 50 mL of deionised water. A separate NaOH solution (1 g/100 mL) was put in a burette and added dropwise with vigorous shaking at room temperature until the mixture turned dark brown and the pH reached 12. They moved for another hour. The precipitate was filtered and washed with ethanol and then repeatedly with deionised water until the filtrate became neutral. The precipitate was dried at 150 °C for 30 min, crushed and finally calcined at 600 °C for 5 h.

Preparation of the Ag_2O/BC composite

The binary composite was prepared by solution processing. For the second sample, biochar (1.0 g) was dispersed in 20 mL of ethanol and Ag2O NPs (0.5 g) in a 50 mL beaker filled with 20 mL of ethanol. The two suspensions were separately sonicated for 30 min at 50 C, mixed and sonicated together for 3 h at 55 C. The slurry was dried at 100 C for 1 h in an oven and the resulting powder (Ag 2 O/BC) was stored under same conditions as the char. The nominal Ag2O loading is 33 wt%.

Characterization

Phase composition was followed by X-ray diffraction on a Siemens D500 diffractometer using Cu K-alpha radiation (lambda = 1.5406 A)

over 2-theta = 10-80 degrees. Crystallite sizes were estimated with the Scherrer relation, D = 0.9 lambda / (beta cos theta), taking beta as the full width at half maximum in radians after correcting for the instrumental contribution. Surface morphology was examined by field-emission scanning electron microscopy (ZEISS, 15 kV, gold-sputtered samples) with an attached energy-dispersive X-ray detector for elemental analysis; the gold peaks arising from the coating were excluded from the quantification. Internal structure was inspected by transmission electron microscopy (Philips CM120) at 100 and 200 nm scale, samples being dispersed in ethanol and dried on carbon-coated copper grids. Surface topography and roughness were measured by atomic force microscopy (DME) in contact mode over scan areas of 1.6 x 1.6 and 2 x 2 micrometres, from which the arithmetic mean roughness Ra, the root-mean-square roughness Rq and the maximum height Rt were extracted. Textural properties were obtained from nitrogen adsorption-desorption isotherms recorded at 77 K (BEL instrument) after degassing at 150 C for 3 h under vacuum; specific surface areas were calculated by the BET method in the relative pressure range 0.05-0.30, total pore volume was taken from the uptake at p/p0 close to 0.99, and the pore size distribution was derived by the BJH method from the adsorption branch. Surface functional groups were identified by FT-IR spectroscopy (Shimadzu, KBr pellets, 400-4000 cm-1) and the optical response was recorded on a double-beam UV-Vis spectrophotometer between 300 and 800 nm using ethanol dispersions. XRD, FE-SEM, EDS, TEM, AFM and BET measurements were performed at the University of Tehran; the remaining analyses were carried out at the University of Diyala.

Model oil and batch adsorption experiments

The model oil was prepared by mixing 10 mL of crude oil with 30 mL of n-hexane in a 500 mL glass flask and stirring on a magnetic hotplate for 1 h to obtain a single homogeneous phase. Its sulfur content, determined before each series, was 2.9 wt%. Batch experiments were carried out in stoppered glass tubes containing 10 mL of the model oil. The adsorbent dose study used 0.1, 0.2, 0.3, 0.4 and 0.5 g at 293 K with a fixed contact time of 60 min. Kinetic runs were carried out with 0.5 g of adsorbent and sampling times of 30, 60, 90, 120 and 150 min, and repeated at 298, 313, 333 and 353 K in a thermostatted water bath. The tubes were sealed to limit hexane loss at the two highest temperatures. The agitation was continuous at a fixed rate. At the conclusion of each interval the material was withdrawn by centrifugation which quickly stops the process and the clean supernatant was tested for residual sulphur. All values are single determinations from freshly prepared solutions.

Data treatment

The removal efficiency and the amount of sulphur adsorbed per unit mass of adsorbent were determined using equations (1) and (2). S_o and S_t are the sulphur levels of the model oil before adsorption and at time t, respectively, in wt%. The analysis is given as a mass fraction of sulphur, and therefore q_t is also stated in those same units here, rather than mg g^{-1}; this avoids bringing an unmeasured solution density into the computation. Four kinetic models in their linear forms were used: pseudo-first-order (3), pseudo-second-order (4), Elovich (5) and Weber–Morris intraparticle diffusion equation (6). Thermodynamic functions were obtained from the distribution ratio $K_c = (S_o - S_e)/S_e$ through the van 't Hoff relation (7) and the Gibbs equation (8).

$$R\ (\%) = [(So - St) / So] \times 100 \quad (1)$$

$$qt = So - St \quad \text{(wt\% sulfur removed per gram of adsorbent basis)} \quad (2)$$

$$\ln(qe - qt) = \ln qe - k1\ t \quad (3)$$

$$t / qt = 1 / (k2\ qe2) + t / qe \quad (4)$$

$$qt = (1/beta) \ln(alpha\ beta) + (1/beta) \ln t \quad (5)$$

$$qt = kid\ t0.5 + C \quad (6)$$

$$\ln Kc = -(dH / R\ T) + (dS / R) \quad (7)$$

$$dG = -R\ T \ln Kc \quad (8)$$

RESULTS AND DISCUSSION

Phase composition

The diffraction patterns are collected in Fi. 1. The Ag_2O sample gave four sharp reflections at 2θ = 38.37, 44.54, 64.66 and 77.58°, indexed as (111), (200), (220) and (311) of a face-centred cubic lattice with a = 4.086 Å. Crystallite sizes from the Scherrer equation ranged between 24.9 and 41.4

nm, with a mean of 30.5 nm.

The char pattern is dominated by a set of sharp lines whose strongest member falls at 29.44 degrees, accompanied by reflections at 23.13, 31.88, 36.04, 39.47, 43.21, 47.50, 48.57 and 57.52 degrees. Taken together these correspond to calcite, CaCO3, retained in the ash fraction of the wood. Superimposed on them is a broad band centred near 23 degrees which is the (002) feature of turbostratic carbon. A char of this kind is therefore a two-phase material: a poorly ordered carbon skeleton carrying crystalline mineral inclusions. Similar mineral phases have been described for chars formed from woody feedstocks at similar temperatures [7, 8].

Both features are present in the composite. Calcite is still dominant at 29.49°. Quartz is found at 26.67°. Four weak lines at 38.24, 44.44, 64.71 and 77.37° indicate the presence of Ag2O. The reflections of Ag_2O are much weaker than in the pure sample, due partially to dilution and partly to the fact that the crystallites are distributed in the carbon matrix. The average crystallite size of the composite was 31.3 nm, which is essentially the same as for the loose particles, indicating that the ultrasonic treatment did not modify the Ag 2 O

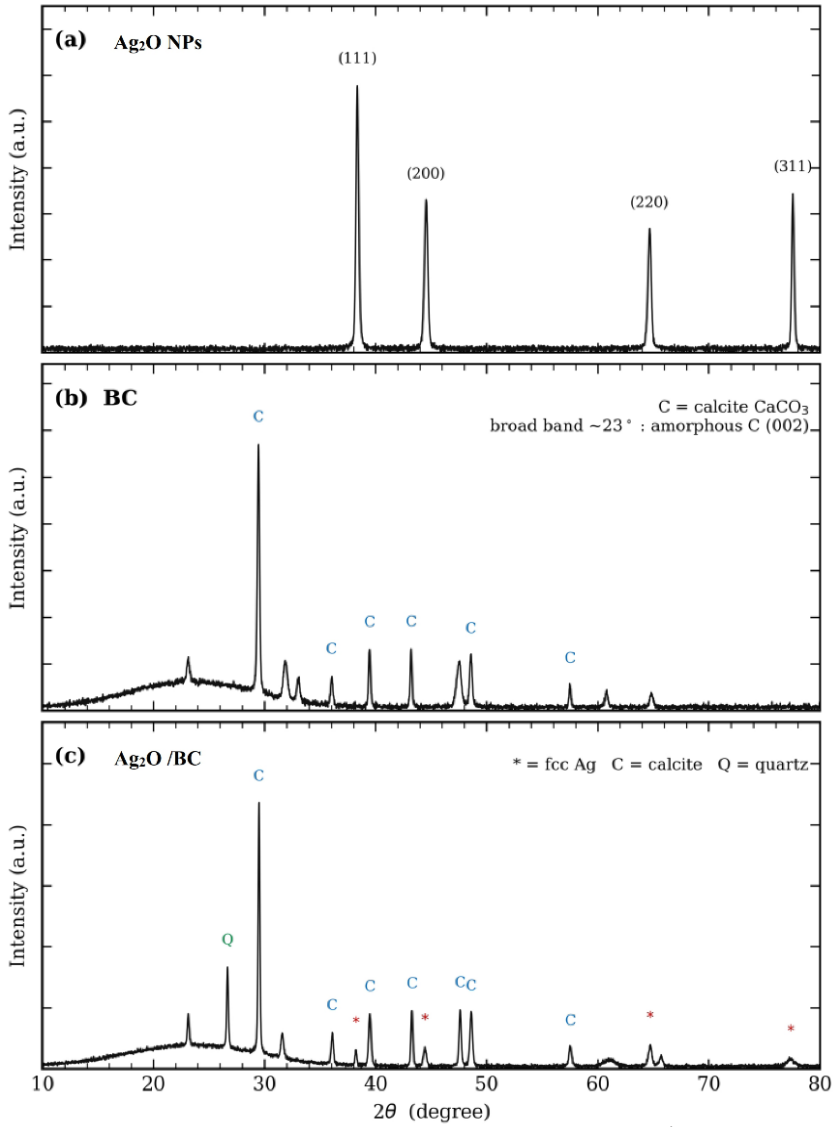

Fig. 1. XRD patterns of (a) Ag_2O NPs, (b) sawdust biochar and (c) the Ag_2O/BC composite. C = calcite, Q = quartz, ♦ = Ag_2O.

domains. Table 1 lists some of the XRD parameters.

Morphology and surface topography

Fig. 2 combines the microscopes. The FE-SEM images show that Ag_2O sample (a) is composed of rounded particles between 38.45 and 66.67 nm that have aggregated into loose clusters, a familiar result of the high surface energy of freshly precipitated metal. The char (b) reveals the predicted image of a pyrolysed lignocellulosic solid: an uneven surface broken up by cavities and channels, with crystalline aggregates in the 28.57–66.67 nm range sitting on the walls. In the composite (c) the Ag_2O particles, 39.96-76.19 nm

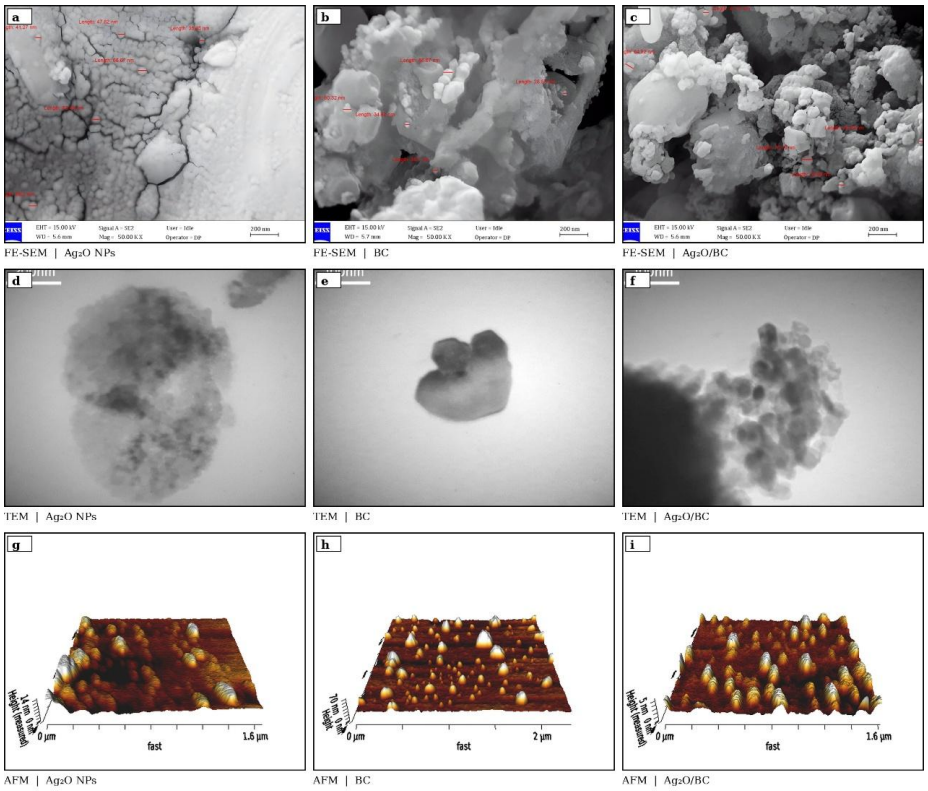

Fig. 2. FE-SEM (a-c), TEM (d-f) and AFM topography (g-i) of Ag_2O NPs, biochar and the Ag_2O/BC composite.

Table 1. Diffraction parameters and Scherrer crystallite sizes of the prepared materials.

Sample	2-theta (deg)	FWHM (deg)	d (A)	(hkl)	D (nm)
Ag_2O NPs	38.365	0.295	2.346	(111)	28.5
	44.543	0.344	2.034	(200)	24.9
	64.661	0.344	1.442	(220)	27.3
	77.578	0.246	1.231	(311)	41.4
BC	23.134	0.295	3.845	C (002), broad	27.5
	29.443	0.246	3.034	calcite (104)	33.4
	39.468	0.197	2.283	calcite (113)	42.9
	43.208	0.197	2.094	calcite (202)	43.4
Ag_2O/BC	26.665	0.197	3.343	quartz (101)	41.5
	29.494	0.197	3.029	calcite (104)	41.7
	38.235	0.197	2.354	Ag (111)	42.7
	44.436	0.295	2.039	Ag (200)	29.1

across, are distributed over the carbon surface and inside some of the wider openings.

The TEM images (d-f) support this reading. Ag_2O appears as dark, electron-dense regions against the lighter carbon background, and in the composite these regions are clearly located on and within the char fragments. Agglomeration is visible in all three samples, which limits how far individual particle boundaries can be traced.

AFM topography (g-i) provides the quantitative counterpart. Arithmetic mean roughness was 1.233 nm for the Ag_2O particles, 4.247 nm for the char and 0.612 nm for the composite; root-mean-square values followed the same order (1.802, 7.096 and 0.831 nm), as did the maximum heights (14.81, 71.94 and 5.581 nm). The composite is thus considerably smoother than either of its components. This is worth noting because a smoother surface is normally associated with the filling of asperities and shallow pores, and it turns out to be consistent with the adsorption behaviour described in section 3.5.

Surface chemistry and optical response

EDS quantification (Fig. 3a) gave 96.2% silver against 3.8% oxygen for the Ag_2O sample. The char contained 67.2% carbon, 25.2% oxygen, 5.8% sulfur and 1.9% nitrogen, a composition typical of a char that has kept a fair amount of its original oxygen functionality. In the composite carbon rose to 95.4% while silver was detected at only 0.4%. That figure is much lower than the 33 wt% loaded, and although EDS is a surface-sensitive technique with a shallow sampling depth, such a large discrepancy suggests that the Ag_2O is unevenly distributed and that much of it has migrated into the pore network rather than remaining on the external surface.

The FT-IR spectra (Fig. 3b) show a broad O-H stretch near 3500 cm-1 in all three materials, weaker in the Ag_2O sample. The char displays bands at 3030 cm-1 (aromatic C-H), around 1070 cm-1 (C-O and C-O-C) and at 596 and 547 cm-1. In the composite the O-H band shifts to 3676 cm-1 and new features appear at 1425, 1114, 597 and 557 cm-1. The shifts in the low-wavenumber region are consistent with an interaction between the Ag_2O and oxygen-containing groups on the carbon surface, although the changes are modest and we would not want to read too much into them.

The optical spectra (Fig. 3c) are more informative. Both the Ag_2O sample and the composite show a well-defined absorption maximum near 425 nm, characteristic of Ag_2O nanoparticles. The absorption peak in the composite is broadened and slightly displaced relative to the free particles, which is consistent with the particles being supported on a strongly absorbing carbon matrix.

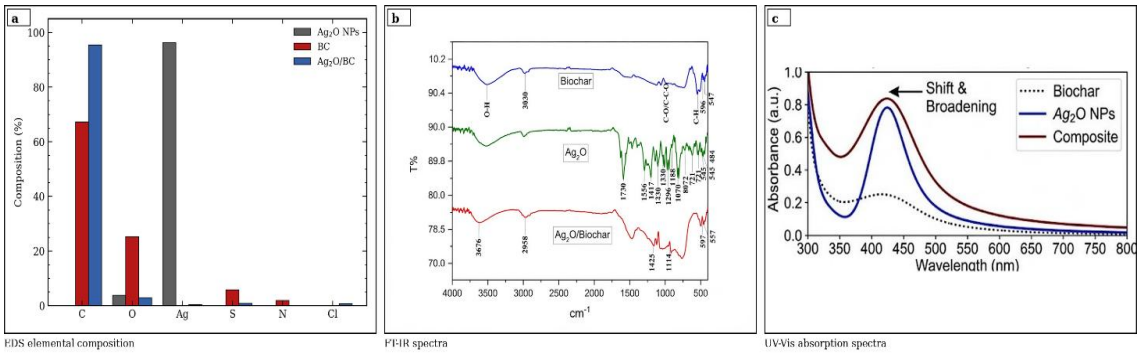

Fig. 3. (a) EDS elemental composition, (b) FT-IR spectra and (c) UV-Vis absorption spectra of the three materials.

Table 2. Textural parameters obtained from nitrogen physisorption at 77 K.

Sample	S_{BET} ($m^2\ g^{-1}$)	$S_{Langmuir}$ ($m^2\ g^{-1}$)	V_{total} ($cm^3\ g^{-1}$)	D_p (nm)
Ag_2O NPs	339.73	470.50	0.1947	2.292
BC	407.23	556.61	0.2302	2.262
Ag_2O/BC	441.02	594.66	0.2459	2.230

Textural properties

Nitrogen isotherms and the corresponding BJH distributions are shown in Fig. 4. All three solids gave a steep uptake at very low relative pressure followed by a long, gently rising plateau, and a narrow hysteresis loop above p/p0 = 0.4 in the case of the Ag_2O NPs and char samples. The shape is intermediate between types I and IV in the IUPAC scheme and indicates a predominantly microporous solid with a mesoporous contribution.

Specific surface areas were 339.7, 407.2 and 441.0 m2 g-1 for Ag_2O NPs, BC and Ag_2O/BC, with total pore volumes of 0.195, 0.230 and 0.246 cm3 g-1 (Table 2). Mean pore widths clustered tightly around 2.3 nm. The composite therefore has the largest area and the largest pore volume of the three, and on that basis alone it would be expected to be the best adsorbent. The pore size distribution of the composite is also the only one that is not monotonic: a secondary shoulder appears between 2 and 3 nm in pore radius, which we take to reflect interstitial voids created where Ag_2O particles rest against the carbon walls.

One point deserves comment. A surface area above 300 m2 g-1 is unusually high for an oxide powder whose crystallites are around 30 nm; for dense spherical Ag_2O of that size the geometric estimate is closer to 20 m2 g-1. The measured

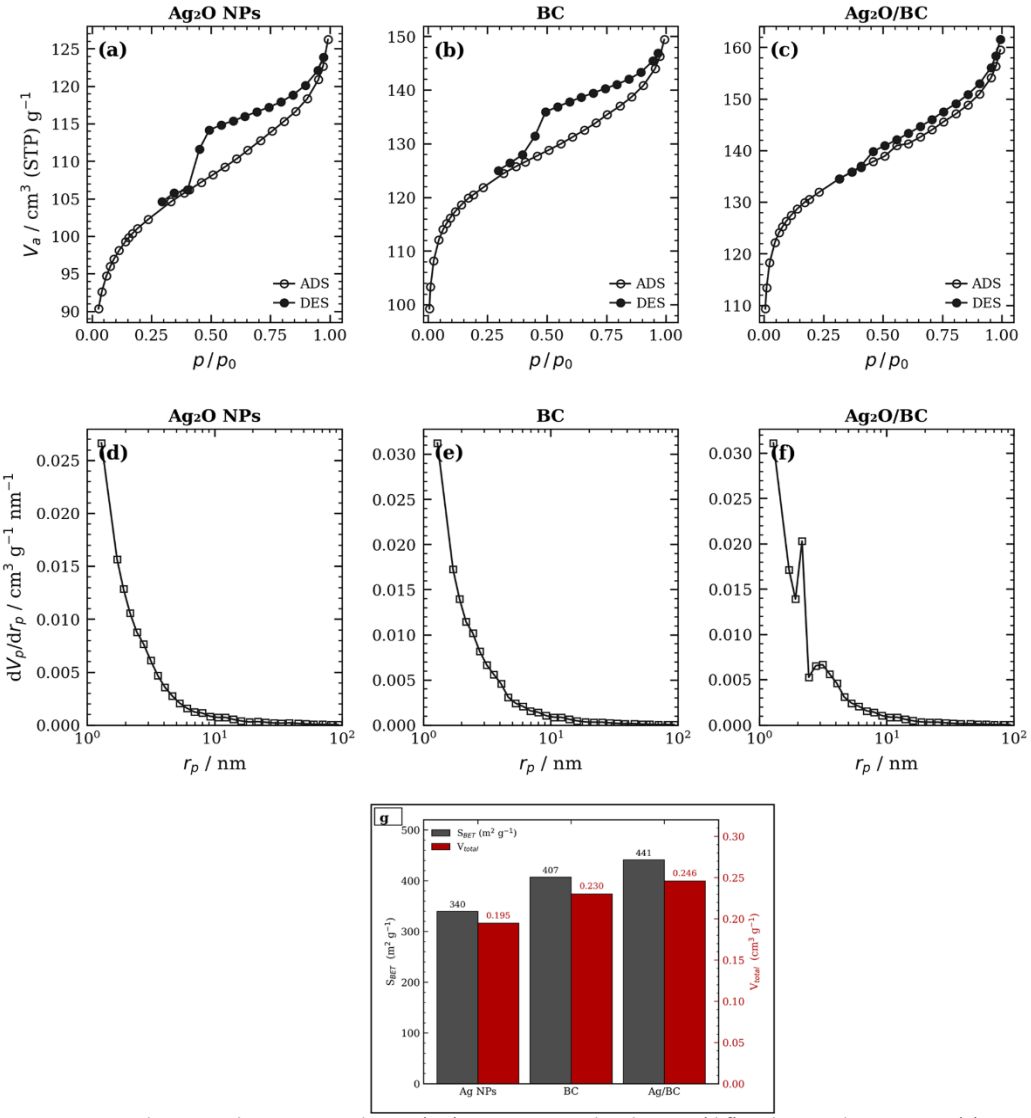

Fig. 4. N2 adsorption-desorption isotherms (a-c), BJH pore size distributions (d-f) and textural parameters (g).

value is therefore not a property of isolated particles but of the porous agglomerate they form, and this should be kept in mind when the area is used to rationalise adsorption capacity.

Effect of adsorbent dose

Removal efficiency rose steadily with adsorbent mass for all three solids (Fig. 5a). Between 0.1 and 0.5 g the char improved from 14.1 to 80.3%, the Ag_2O NPs from 16.2 to 65.9% and the composite from 3.1 to 47.9%. The trend is the usual one and follows from the increase in available sites, but the curves begin to flatten between 0.4 and 0.5 g, which suggests that the system is approaching saturation. A dose of 0.5 g in 10 mL was adopted for the remaining experiments.

The ranking, BC > Ag_2O NPs > Ag_2O/BC, was the same at every dose. It is the reverse of what the BET data would predict and it persisted through the whole study, so it cannot be dismissed as scatter in a single series.

Effect of contact time and temperature

The influence of contact duration on the removal efficiency was examined at 293 K for a fixed dose of 0.5 g (Fig. 5b). Uptake significantly increased in the first 60 min and then tapered down. By 150 min the char had reached 85.9%, Ag 2 O NPs 68.3% and the composite 52.1%. None of the curves had flattened out at 150 min, so equilibrium was approached rather than achieved and the 150 min values are used here as operational equilibrium points. The order was the same at each sampling period (BC > Ag 2 O NPs > Ag 2 O/BC), and was consistent with the dose series.

The effect of temperature was studied

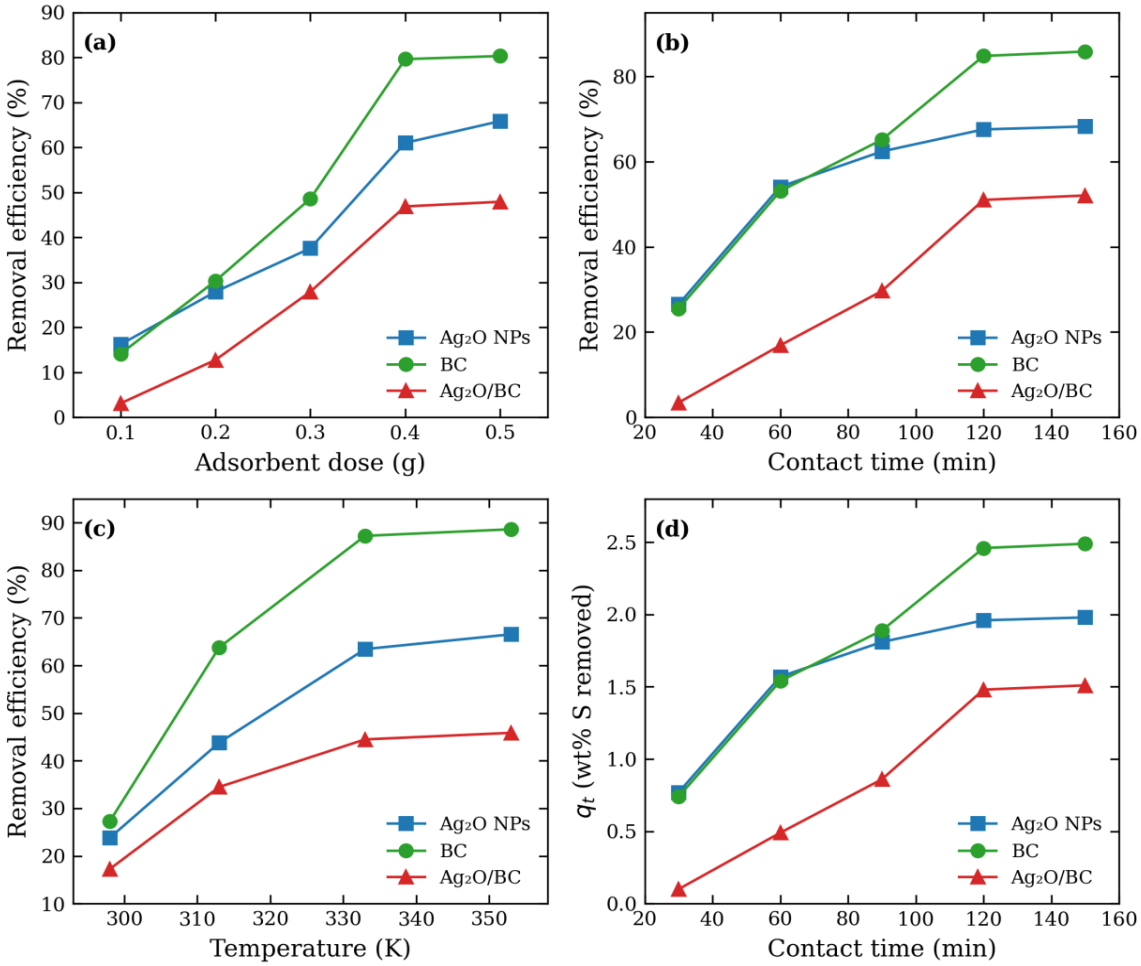

Fig. 5. (a) Effect of adsorbent dose at 293 K and 60 min; (b) removal against contact time at 293 K; (c) effect of temperature at 60 min; (d) uptake (q_t) against contact time at 293 K.

individually by fixing the contact duration as 60 min and dose as 0.5 g and altering the temperature from 298 to 353 K (Fig. 5c). Removal was enhanced with temperature for all three solids. The biochar grew from 27.2% at 298 K to 88.6% at 353 K, Ag2O NPs from 23.8% to 66.6% and composite from 17.2% to 45.9%. The increment between 333 and 353 K was small for the char (87.2 to 88.6%) but more relevant for the Ag2O NPs (63.4 to 66.6%) suggesting the char reaches saturation at its 60 min equilibrium, while the Ag2O NPs still have capacity to be filled.

There are presumably two effects that contribute to the temperature dependence. Higher temperature means reduced viscosity of the hexane–crude mixture, and therefore higher diffusion and better ability of molecules to overcome the energy barrier for entering the small pores. The average pore width obtained here is about 2.3 nm and the kinetic diameter of

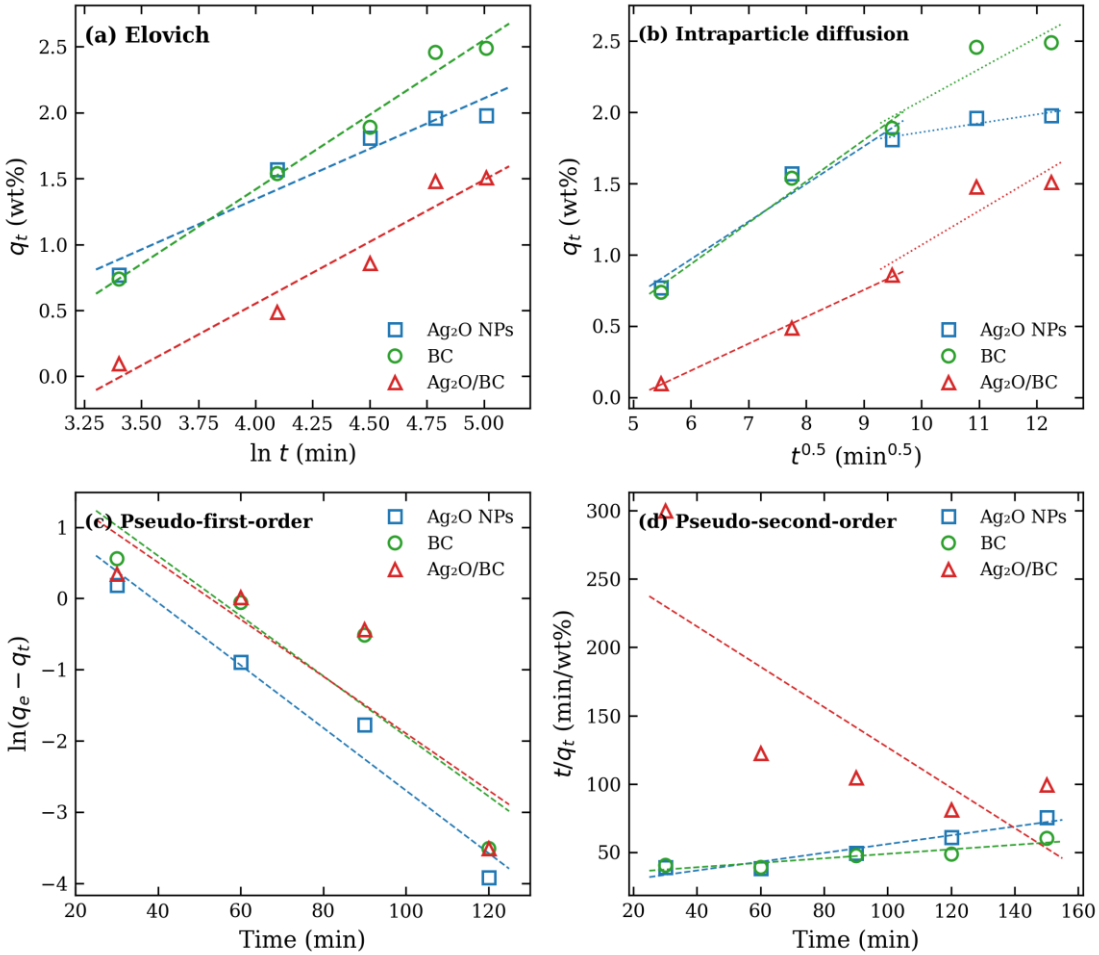

Fig. 6. Linearised kinetic plots at 293 K: (a) Elovich, (b) intraparticle diffusion with two stages separated, (c) pseudo-first-order and (d) pseudo-second-order.

Table 3. Kinetic parameters of the three adsorbents at 293 K (q_t in wt% sulfur removed).

Sample	qe,exp	k1 (min^{-1})	qe,cal (PFO)	R^2 (PFO)	k2	qe,cal (PSO)	R^2 (PSO)	α	β	R^2 (Elov.)
Ag_2O NPs	1.980	0.044	5.48	0.957	0.0044	3.11	0.922	0.081	1.31	0.937
BC	2.490	0.042	9.85	0.818	0.0008	6.10	0.850	0.073	0.88	0.983
Ag_2O/BC	1.510	0.040	8.22	0.766	0.0079	−0.68	0.607	0.031	1.07	0.936

Columns 3–5 pseudo-first-order, 6–8 pseudo-second-order, 9–11 Elovich.

dibenzothiophene is about 0.9 nm, so entry to the interior is possible though not without hindrance. It is worth noting that the maximum temperature investigated, 353 K, is above the normal boiling point of n-hexane. The tubes were sealed for these runs, but a tiny loss of solvent cannot be fully excluded and the 353 K points should be considered with more caution than the others.

Adsorption kinetics

The kinetic constants for the three adsorbents at 293 K are presented in Table 3 and the linearised fits are displayed in Fig. 6. Four models were compared to each other. The quantity adsorbed at each time point, q t , was computed directly from the removal data as q t = S 0 x R(%)/100, yielding values in wt% sulphur removed.

The pseudo second order model was not fitted well. The correlation coefficient was 0.92 for the Ag 2 O NPs and 0.85 and 0.61 for the char and composite, respectively. The equilibrium capacity of the composite was calculated to be negative (−0.68 wt%) which has no physical meaning but indicates simply a negative slope in the t /q tplot. The pseudo-first-order model returned somewhat higher R^2 values (0.96 for Ag, 0.82 for BC, 0.77 for Ag_2O/BC) but the calculated capacities exceeded the measured ones by factors of 2.8 to 5.4, so it cannot be regarded as an adequate description either.

The Elovich equation gave the most consistent picture. For the biochar, $R^2 = 0.983$ with $\alpha = 0.073$ wt%/min and $\beta = 0.88$ $(wt\%)^{-1}$. The Ag_2O NPs gave $R^2 = 0.937$ ($\alpha = 0.081$, $\beta = 1.31$) and the composite $R^2 = 0.936$ ($\alpha = 0.031$, $\beta = 1.07$). Elovich behaviour is normally taken to indicate adsorption onto an energetically heterogeneous surface, with the activation energy for adsorption rising as coverage increases. That is a reasonable description of a char carrying oxygenated groups, mineral inclusions and a wide distribution of pore sizes. The lower α for the composite reflects its restricted access to pore interiors, consistent with the pore-blocking interpretation developed below.

The disagreement with the pseudo-second-order result is worth dwelling on. A model that fails for three different solids is unlikely to be failing by accident. What the t/q_t plots actually show is that uptake continues to change appreciably after 90 min, so the linearisation, which is heavily weighted towards the long-time points, has nothing stable to anchor to.

Diffusion analysis

Weber–Morris plots of q_t against $t^{0.5}$ (Fig. 6b) were not linear through the origin, ruling out intraparticle diffusion as the sole rate-controlling step. Two distinct regions could be separated in each case: a first stage covering 30–90 min and a second covering 90–150 min. Parameters for both stages are given in Table 4.

For the Ag_2O sample the first-stage diffusion coefficient was about four times larger than the second (kid,1/kid,2 = 4.2), the pattern expected when rapid external mass transfer is followed by slower migration into the pore network. The biochar showed a ratio of 1.3, indicating that the two stages were of comparable magnitude and that pore diffusion was not markedly slower than the external step. The ratio for the composite was less than the unity (0.79) which indicates that the second stage was faster than the first one. This is not normal and we consider it as an induction period. The Ag2O NPs deposits block the pore mouths, such that early uptake is limited to the exterior surface, and only after the outer layer has been populated does transport into the interior become important.

Intercepts were negative for biochar (−0.81 and −0.13) and for the first stage of all three materials. A negative C in this model indicates that the fitted line extrapolates below zero at t = 0, the signature of a lag before measurable uptake begins. At −0.94, the composite had the most negative first-stage intercept of the three, again indicating restricted early access. Taken with the two-stage structure, the picture that emerges is of a process controlled jointly by film diffusion and pore diffusion, with

Table 4. Two-stage Weber–Morris intraparticle diffusion parameters (Stage I: 30–90 min; Stage II: 90–150 min).

Sample	kid,1	C1	R^2	kid,2	C2	R^2	kid,1/kid,2
Ag_2O NPs	0.264	−0.615	0.950	0.063	1.236	0.863	4.22
BC	0.290	−0.806	0.979	0.221	−0.130	0.817	1.31
Ag_2O/BC	0.189	−0.945	0.996	0.240	−1.328	0.814	0.79

neither dominating throughout.

Thermodynamic functions

The distribution ratio Kc = R%/(100 − R%) was computed from the temperature series at 60 min contact time. Van 't Hoff plots (Fig. 7a) gave enthalpy changes of 30.0, 49.3 and 21.7 kJ mol^{-1} for the Ag_2O NPs, char and composite respectively, confirming that uptake is endothermic in every case. All three values lie below the 40 kJ mol^{-1} conventional boundary between physisorption and chemisorption, except for the biochar, whose value of 49.3 kJ mol^{-1} suggests a contribution from specific chemical interactions between the sulfur-bearing aromatics and the oxygen-containing functional groups on the carbon surface.

Entropy changes were positive throughout (92.5, 160.1 and 61.8 J mol^{-1} K^{-1}). Positive entropy in a liquid-phase adsorption is generally attributed to the release of solvent molecules from the surface as the larger sulfur species take their place, which more than compensates for the loss of translational freedom by the adsorbate. The large ΔS for the char is consistent with its high surface roughness and complex pore system, which would involve more solvent displacement per adsorption event.

Gibbs energies were calculated independently as ΔG° = −RT ln Kc at each temperature (Table 5, Fig. 7b). The biochar is the only material for which ΔG° becomes negative above 313 K, reaching −6.0 kJ mol^{-1} at 353 K. For the Ag_2O NPs, ΔG° crosses zero between 333 and 353 K, and for the composite it remains positive at all four temperatures, indicating that adsorption onto Ag_2O/BC is not spontaneous under the conditions used here. This is a further expression of the pore-blocking penalty discussed below.

It should be observed that the van 't Hoff R^2 values (0.84–0.92), which are sufficient for determining the sign and rough magnitude of ΔH, are somewhat spread out for four data points. The 353 K point is above the boiling point of n-hexane and has the greatest influence on both the slope and the intercept. For example, deleting the 353 K point from the biochar fit decreases ΔH from 49.3 to around 19 kJ mol -1 and increases R 2 to 0.99. Thus, the thermodynamic parameters should be considered just as indicative and not exact.

Why the composite underperforms, and comparison with earlier work

Why the composite underperforms is the central question raised by these results. Four observations point in the same direction. Its BET area is the largest of the three, so the loss cannot

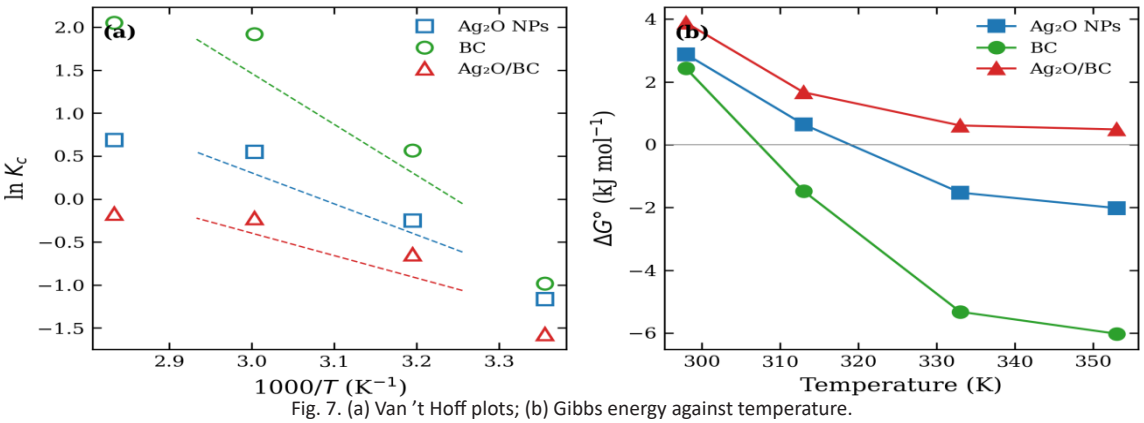

Fig. 7. (a) Van 't Hoff plots; (b) Gibbs energy against temperature.

Table 5. Thermodynamic functions derived from the temperature series (60 min, 0.5 g).

Sample	ΔH (kJ/mol)	ΔS (J/mol·K)	R^2	ΔG 298	ΔG 313	ΔG 333	ΔG 353
Ag_2O NPs	30.0	92.5	0.922	+2.88	+0.65	−1.53	−2.02
BC	49.3	160.1	0.906	+2.43	−1.47	−5.32	−6.02
Ag_2O/BC	21.7	61.8	0.838	+3.89	+1.67	+0.61	+0.49

Gibbs energies in kJ mol^{-1}, calculated from ΔG° = −RT ln Kc.

Table 6. Comparison of the present adsorbents with recently reported desulfurization systems.

Adsorbent	Feed	S content	Removal (%)	Reference
K2CO3-activated biochar (date/olive stones)	Real gasoline	n.r.	88.1	[1]
CuO-activated biochar (date pits)	Real gasoline	n.r.	84.2	[5]
Activated biochar (date pits)	Real gasoline	n.r.	80.1	[5]
KOH-biochar (date stones/walnut shells)	DBT in n-hexane	300 ppm	97.8	[6]
Cashew nut shell activated carbon	Kerosene	189.7 ppm	80.9	[11]
Cashew nut shell activated carbon	Diesel	189.7 ppm	71.8	[11]
Carbonized corncob	DBT in n-hexane	400 ppm	75.0	[10]
Ag/ZnO NPs on activated carbon	DBT in hexane-toluene	250 ppm	99.0	[16]
AgNP-coated membrane reactor	Crude oil model	n.r.	70-79	[17]
Ag NPs on Eichhornia crassipes	DBT in n-heptane	n.r.	~85	[20]
Sawdust biochar (this work)	Basra crude / n-hexane	2.9 wt%	88.6	–
Ag_2O NPs (this work)	Basra crude / n-hexane	2.9 wt%	66.6	–
Ag_2O/BC composite (this work)	Basra crude / n-hexane	2.9 wt%	45.9	–

n.r. = not reported. Removal values for the present work are at 353 K, 0.5 g and 60 min.

be attributed to a reduction in total surface. Its AFM roughness is the lowest, indicating that surface irregularities have been filled in. Its intraparticle diffusion behaviour is inverted relative to the other materials, with the slow step coming first. And at every temperature, its ΔG° is the least favourable of the three. The most economical explanation is that the Ag_2O particles, which are 40–76 nm across, sit at and partly occlude the entrances to a pore system whose mean width is only about 2.3 nm. Nitrogen, a small molecule at 77 K, still reaches the interior and registers a high area; the much larger sulfur-bearing aromatics do not.

There is a second possibility that cannot be separated with the present data. The EDS result of 0.4% silver in the composite is far below the nominal 33 wt% loading, which may mean that a substantial part of the Ag_2O was lost during the ultrasonic treatment and subsequent handling. If so, the composite would combine a diluted carbon phase with only marginal Ag_2O functionality, and would be expected to fall between the two components rather than below both. Since it falls below both, pore blocking remains the more likely primary cause, but a lower effective loading may contribute.

Table 6 places the present results alongside recent work. Direct comparison is complicated because most published studies use dilute model fuels containing a single sulfur compound at a few hundred ppm, whereas the feed used here is a real crude at 2.9 wt%, roughly two orders of magnitude more concentrated. Against that background, 88.6% removal at 353 K (60 min) or 85.9% at 293 K (150 min) from an untreated crude at 2.9 wt% sulfur, using a char made from waste sawdust with no chemical activation, is a respectable result.

CONCLUSION

Biochar prepared from sawdust at 700 °C removed up to 88.6% of the sulfur present in a Basra crude oil model at 353 K and 60 min contact time, and 85.9% at 293 K and 150 min. It outperformed both Ag_2O nanoparticles and the Ag_2O/BC composite at every dose, contact time and temperature examined. Loading Ag_2O onto the char raised the BET surface area to 441 $m^2\ g^{-1}$ yet lowered uptake, an outcome we attribute to blockage of pore entrances whose mean width is close to 2.3 nm. Kinetics at 293 K were best described by the Elovich equation (R^2 = 0.94–0.98), while the pseudo-second-order model gave poor fits and physically meaningless parameters. Weber–Morris analysis separated a film diffusion stage from a pore diffusion stage, with the composite showing an inverted sequence consistent with obstructed pore mouths. Thermodynamic analysis of the temperature series (298–353 K) confirmed endothermic uptake for all three materials (ΔH = 21.7–49.3 kJ mol^{-1}). Biochar was the sole adsorbent with a negative ΔG° higher than 313 K. The practical message is that a simple, unactivated char from a waste feedstock is a suitable desulfurization adsorbent for heavy Iraqi crude and that adding a metal oxide phase is not inherently an improvement.

ACKNOWLEDGEMENT

We are grateful to the University of Babylon for its help in completing the research.

CONFLICT OF INTEREST

The authors declare that there is no conflict of interests regarding the publication of this manuscript.

REFERENCES

1. Saeed SK, Altamer DH, Khalaf AM, Fadhil AB. Ultrasound-assisted adsorptive desulfurization of dibenzothiophene from model fuel on K_2CO_3-activated biochar. Chemical Engineering and Processing - Process Intensification. 2024;206:110065.
2. Saha B, Vedachalam S, Dalai AK. Review on recent advances in adsorptive desulfurization. Fuel Process Technol. 2021;214:106685.
3. Yeole NR. An overview of adsorptive desulfurization of liquid transportation fuels over various adsorbents including zeolites. Environmental Progress and Sustainable Energy. 2022;42(1).
4. Sarkarabad KM, Shayanmehr M, Ghaemi A. Optimization and modeling of sulfur removal from liquid fuel using carbon-based adsorbents through synergistic application of RSM and machine learning. Scientific Reports. 2025;15(1).
5. Al-Irhayim AN, Ahmed NH, Al-Layla NMT, Fadil AB. Synthesis of Nano Copper Oxide Functionalized Date Pits- Derived Microporous Activated Biochar and Its Application in the Adsorptive Desulfurization of Model and Real Fuel Oils. Chemistry and Chemical Technology. 2026;20(1):126-141.
6. Alyawer Ameen L, Altamer Marwa H, Khalaf Ahmed M, Al-Omari Amena F, Fadhil Abdelrahman B. Adsorption Desulfurization of Liquid Fuel Using a Blend of Date Stones and Walnut Shells by Box–Behnken Design. Asia-Pacific Journal of Chemical Engineering. 2025;21(2).
7. Uzunova S, Minchev L, Uzunov I. Modelling of Aromatic Sulfur Compounds Adsorption from Hydrocarbon Fuels by Biochar Based Adsorbent. IOP Conference Series: Earth and Environmental Science. 2022;987(1):012002.
8. Urgel JJDT, Briones JMA, Diaz EB, Dimaculangan KMN, Rangel KL, Lopez ECR. Removal of diesel oil from water using biochar derived from waste banana peels as adsorbent. Carbon Research. 2024;3(1).
9. Yaseen M, Ullah S, Ahmad W, Subhan S, Subhan F. Fabrication of Zn and Mn loaded activated carbon derived from corn cobs for the adsorptive desulfurization of model and real fuel oils. Fuel. 2021;284:119102.
10. Oday Y, Aljendeel H, Nidhal Shareef Z. Preparation and characterization of adsorptive carbonized corncob for elimination of sulfur from sulfurized n-hexane. Iraqi Journal of Chemical and Petroleum Engineering. 2025;26(2):47-56.
11. Mwasamila FA, Mushi SJ, Mabeyo PE. The potential of agricultural wastes-based adsorbent for desulfurization of petroleum fractions. Journal of Sulfur Chemistry. 2026;47(3):443-476.
12. Othman CS, Salih YM, Hamasalih LO, Saleem HJ. Influence of different nanocomposite carbon-based adsorbers on the adsorption desulfurization of dibenzothiophene in model oil and diesel fuel: a comparative study. Reaction Kinetics, Mechanisms and Catalysis. 2023;136(2):919-936.
13. Othman CS, Salih YM, Hamasalih LO. Adsorption desulfurization of dibenzothiophene in a model and diesel fuel by hybrid activated charcoal/mixed metal oxide. Pet Sci Technol. 2022;41(22):2121-2140.
14. Sh. Ali I, Yasin Thayee Al-Janabi O, Al-Tikrity ETB, Foot PJS. Adsorptive desulfurization of model and real fuel via wire-, rod-, and flower-like Fe_3O_4@MnO_2@activated carbon made from palm kernel shells as newly designed magnetic nanoadsorbents. Fuel. 2023;340:127523.
15. Omar RA, Verma N, Arora PK. Sequential desulfurization of thiol compounds containing liquid fuels: Adsorption over Ni-doped carbon beads followed by biodegradation using environmentally isolated Bacillus zhangzhouensis. Fuel. 2020;277:118208.
16. Saleem HJ, Salih YM, Hamasalih LO, Othman CS. Application of green synthesis nanocomposite adsorbents in the adsorption desulfurization of dibenzothiophene in model oil. Journal of Sulfur Chemistry. 2023;44(4):416-431.
17. Suliman MH, Basheer C, Siddiqui MN, Al-Arfaj AA. Biosynthesized Silver Nanoparticles Decorated Electro-Membrane Flow Reactor an Effective Tool for the Desulfurization of Fuels. Arabian Journal for Science and Engineering. 2022;47(1):543-550.
18. Li T, Li X, Wu H, Chen Q. Design of a Recyclable Photoresponsive Adsorbent via Green Synthesis of Ag Nanoparticles in Porous Aromatic Frameworks for Low-Energy Desulfurization. Molecules. 2026;31(2):248.
19. Ren M, Fan F, Zhou B, Liang X, Yang Z. Dynamic simulation of adsorption desulfurization from diesel fuel over activated carbon in the fixed bed. Chem Eng Res Des. 2022;183:274-284.
20. Salim A, Al-Haidarie Y, Nasir M. Adsorptive Desulfurization of Model Oil by Ag nanoparticles-modified Eichhornia crassipes: Equilibrium, Kinetics, and Thermodynamic Studies. Egyptian Journal of Chemistry. 2022;0(0):0-0.
21. Khosravi-Nikou MR, Safari MH, Rad AA, Hassani P, Mohammadian M, Ahmadi M, et al. Desulfurization of liquid fuels using aluminum modified mesoporous adsorbent: towards experimental and kinetic investigations. Scientific Reports. 2021;11(1).
22. Humadi JI, Hamad KI, Abdulkareem HA, Ismael MN, Jarullah AT, Ahmed MA, et al. Eco-Friendly Oxidative–Adsorptive Desulfurization for Real Diesel Fuel Using Green MnO2 Biowaste-Extracted Calcite in Digital Basket Reactor. Processes. 2025;13(10):3084.
23. Li Y, Xu Y, Huang E, Kong L, Zeng Y. Efficient adsorption desulfurization via encapsulation of CeO_2 nanoparticles in hierarchical porous HKUST-1. J Colloid Interface Sci. 2025;689:137237.
24. Chen K, Li W, Biney BW, Li Z, Shen J, Wang Z. Evaluation of adsorptive desulfurization performance and economic applicability comparison of activated carbons prepared from various carbon sources. RSC Advances. 2020;10(66):40329-40340.
25. Nawaf AT, Hameed SA, Abdulateef LT, Jarullah AT, Kadhim MS, Mujtaba IM. A Novel Synthetic Nano-Catalyst (Ag_2O_3/Zeolite) for High Quality of Light Naphtha by Batch Oxidative Desulfurization Reactor. Bulletin of Chemical Reaction Engineering and Catalysis. 2021;16(4):716-732.
26. Yari A, Abdolmaleki A. Utilization of silver-modified ostrich eggshell membrane in pervaporation for liquid fuel desulfurization. Chemical Engineering Journal Advances. 2026;26:101074.
27. Alwan HH. Oxidative desulfurization of a model fuel using MoO3 nanoparticles supported on carbon nanotubes catalyst: Examine most significance variables, optimization, kinetics and thermodynamics study. South African Journal of Chemical Engineering. 2022;40:230-239.
28. Louis M, Behera P, Sorokhaibam LG. Magnetic iron nanoparticles (Fe_3O_4) supported on activated carbon as a

hybrid adsorbent for desulphurisation of liquid fuels. Int J Environ Anal Chem. 2021;103(11):2659-2680.
29. Maxim F, Stoian GS, Toma EE, Borca CN, Müller Gubler EA, Atkinson I, et al. Carbon-supported ZnO materials for sulfur capturing in supercritical water. Scientific Reports. 2025;15(1).
30. Matloob AM, Abd El-Hafiz DR, Saad L, Mikhail S. Hybrid Nanoarchitectonics with Cr, Fe-MOF/ Graphene Nanocomposite for Removal of Organic Sulfur Compounds from Diesel Fuel. Journal of Inorganic and Organometallic Polymers and Materials. 2022;33(1):254-265.
31. Rezvani MA, Khandan S, Rahim M. Synthesis of $(Gly)_3PMo_{12}O_{40}$@$MnFe_2O_4$ organic/inorganic hybrid nanocomposite as an efficient and magnetically recoverable catalyst for oxidative desulfurization of liquid fuels. International Journal of Energy Research. 2021;46(3):2617-2632.
32. Liu Y, Zuo P, Yin X, Li C, Zhao F, Shi h, et al. Ultra-deep oxidative desulfurization of high sulfur liquid fuels using W/W2C heterostructured nanoparticles embedded on N-doped graphene. Journal of Environmental Chemical Engineering. 2024;12(2):112173.